

Thermal Optofluidics: Principles and Applications

Jiajie Chen, Jacky Fong-Chuen Loo, Dongping Wang, Yu Zhang, Siu-Kai Kong, and Ho-Pui Ho*

Thermal optofluidics is an emerging field that promises to create numerous research and application opportunities in biophysics, biochemistry, and clinical biology. Innovation in plasmonic optics has led to the development of various invaluable tools in the fields of biosensing and microfluidic manipulation. The optothermal effect originates from light–matter interactions during photon–phonon conversion, which can lead to micro- or nanoscale inhomogeneities in the thermal distribution. This further induces a series of hydrodynamic phenomena such as natural convection, Marangoni convection, thermophoresis, the electrolyte Seebeck effect, depletion forces, and interfacial effects in colloidal particles. Light–matter interactions are particularly important for three aspects of microfluidics, namely the motion of colloidal particles, fluidic actuation, and biochemical reactions. This review first systematically elucidates the role of both nanoscale plasmonic thermal generation and heat-induced fluidic motion in optofluidic microsystems. Then, recent state-of-the-art thermal optofluidic applications of the above-listed three aspects are presented. The paper aims to provide an insightful reference for future research in optofluidic biochemical systems.

1. Introduction

The synergistical integration of optics and microfluidics has led to the rapid development of optofluidic systems, which in turn have created many application opportunities within the biological sciences. The field of optofluidics that was emerged in 2003 contains generally two key technology components:^[1,2] i) photonics, in which the light propagation is manipulated by fluidic materials^[3] and ii) microfluidics, in which light is used to manipulate a microfluidic system for colloidal particles control, fluidic actuation, or bioapplications.^[4] This paper is mainly focused on the latter one, in which the optothermal effect of plasmonic optics has played substantial roles in recent studies. Plasmonic nanostructures allow the coupling of electromagnetic fields at subwavelength scale^[5,6] and enable new sensing and hydrodynamic functionalities previously unachievable, especially in biochemical optofluidic applications.^[4,7–9]

The superior efficiency of photon–phonon conversion induces powerful sub-micrometer scale thermodynamic process that can perturb microfluidic systems. Plasmonic nanostructures can serve as highly efficient, size-dependent, and wavelength-tunable optothermal nanoconvertors to tailor the temperature distribution on the nanoscale. The heating effect becomes significant when the incident light frequency meets the plasmon resonant conditions.^[10–12] Its heat generation is originated from Joule heating, creating an abrupt temperature gradient near the surface.^[13,14] Richardson et al. showed that the efficiency (η) of light-to-heat conversion by a colloidal suspension of 20 nm gold particles is close to 1 ($0.97 < \eta < 1.03$).^[15] The time scale to reach a steady-state temperature distribution of the photothermal effect is in sub-microseconds level.^[14] A quantitative study by Chen et al. showed that nanostructures excited by a critical light pulse can be heated from room temperature to 795 K in 4 ns.^[16] Therefore, the unique temporal and spatial property of plasmonic temperature gradient can lead to various intriguing micro and nanoscale optothermal–hydrodynamic phenomena, such as Rayleigh–Benard-like fluid convection,^[17] Marangoni convection,^[18–20] thermophoresis,^[21–23] the Seebeck effect,^[24] depletion forces,^[25,26] interfacial effects in colloidal particles,^[27–29] and other interactions. To comprehensively understand optothermal effects, researchers have focused on the origins of heat and thermodynamic motion on the nanoscale, providing useful guidance for thermal optofluidic

Dr. J. J. Chen
Key Laboratory of Optoelectronic Devices and Systems of Ministry of Education and Guangdong Province
College of Optoelectronic Engineering
Shenzhen University
Shenzhen 518060, China

Dr. J. F.-C. Loo, Prof. H.-P. Ho
Department of Biomedical Engineering
The Chinese University of Hong Kong
Shatin 999077 Hong Kong SAR, China
E-mail: aaron.ho@cuhk.edu.hk

Dr. D. P. Wang
Department of Mechanical and Automation Engineering
The Chinese University of Hong Kong
Shatin 999077 Hong Kong SAR, China

Dr. Y. Zhang
Department of Electronics and Communication Engineering
Shenzhen Polytechnic
Shenzhen 518055, China

Prof. S.-K. Kong
Biochemistry Programme
School of Life Sciences
The Chinese University of Hong Kong
Shatin 999077 Hong Kong SAR, China

 The ORCID identification number(s) for the author(s) of this article can be found under <https://doi.org/10.1002/adom.201900829>.

The copyright line for this article was changed back to Wiley-VCH on 23 November 2020 because open access order was cancelled.

DOI: 10.1002/adom.201900829

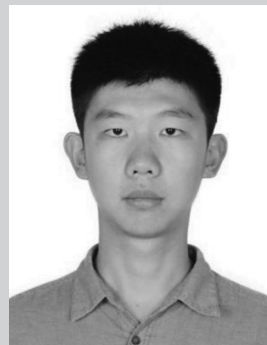
applications. These applications are mainly divided into three categories discussed next.

1.1. Manipulation of Colloidal Particles

The plasmonic tweezer technique, first developed in 2007,^[30] has been explored extensively for its abilities of sub-diffraction-limited and nanoscale manipulation.^[31–33] However, the thermodisturbance caused by plasmonic thermal heating has long been a major drawback restricting the potential use of plasmonic trapping. Various techniques including self-induced back-action trapping,^[34] integration of heat sinks,^[35] and drastic reduction of sample chamber thickness^[36] have been used to alleviate such thermal effects. Despite the issue of thermodisturbance, optothermal effects have been demonstrated in several trapping experiments in the past 5 years, including plasmonic nanoantenna-assisted trapping with an AC electric field^[37] and trapping in a thermally absorptive medium.^[38] Additionally, Kang et al. utilized the plasmonic optothermophoretic effect to perform optical manipulation in a microfluidic platform.^[39,40] Thermophoresis-assisted tweezers have also been studied extensively for applications such as trapping particles on a gold-nanostructure-decorated fiber tip,^[41] microscale electric thermal heater (METH) tweezers without optical assistance,^[42,43] biomaterial manipulation,^[44,45] and manipulation and assembly of plasmonic nanoparticles.^[46–48]

1.2. Optofluidic Actuation

In ordinary optofluidic systems, microscale surface tension becomes the dominant force due to the low Reynolds number in a microfluidic channel. Extensive efforts have been made to resolve three major challenges of optofluidic actuation systems: flow pumping, fluidic valving, and sample mixing. For sample mixing, both optofluidic mixing in a microchannel^[49,50] and the use of optically controlled microfluidic valves via material phase changing^[51,52] have been investigated. In 2006, Liu et al. achieved fluidic control via optical-to-hydrodynamic energy conversion by suspended photothermal nanoparticles near the liquid–air interface.^[53] Chen et al. then improved this technique by using photothermal conversion and surface tension to control gold nanostructures beneath the fluidic channel instead of suspended photothermal particles,^[54] providing a possible solution to all three challenges in one microfluidic system. In addition, the powerful hydrodynamic phenomenon of microbubbles can be produced to enhance optofluidic systems due to their high optothermal conversion efficiency.^[20,55–57] Microbubbles have found a range of applications in microfluidic systems, including the prominent ability to induce strong Marangoni convection by creating an uneven thermal distribution at the liquid–air interface to support long-range actuation and particle transportation.^[18,56,58] Because it can be used to manipulate microfluids in a noncontact manner, optofluidic actuation has a unique ability to enhance the sensing performance of microfluidic systems and simplify their design.



Jiajie Chen received his B.Sc. in optoelectronics from Nankai University in 2012 and obtained his Ph.D. in electronic engineering from the Chinese University of Hong Kong in 2016. Since then, he has been working as a postdoctoral fellow in the Chinese University of Hong Kong and University of California San Diego. In 2019, he joined Shenzhen University as an assistant professor. His research interests include optofluidics, surface plasmon resonance biosensors and optical tweezers.



Jacky Fong-Chuen Loo has obtained a Ph.D. degree in biochemistry and is currently a postdoctoral fellow in the Department of Biomedical Engineering in Hong Kong. He focuses on the development of nanophotonics and microfluidics techniques and integrates the know-how in point-of-care biosensors for healthcare applications. He is also an advisor in startup companies, consulting on the solution for biomedical applications in different fields.



Ho-Pui Ho received his B.Eng. and Ph.D. in electrical and electronic engineering from the University of Nottingham in 1986 and 1990, respectively. He is now a professor in the Department of Biomedical Engineering, The Chinese University of Hong Kong. His research interests include nanomaterials for photonic and sensor applications, surface plasmon resonance biosensors, nanophotonics, optical instrumentation, and lab-on-a-disc.

1.3. Optothermally Assisted Bioapplications

Optothermal microfluidic techniques have had a significant impact on physiological and clinical use in recent years. The optothermal microfluidic has enabled living cell trapping and manipulations, where plasmonic heat-induced natural convection and thermophoresis provides a larger manipulation

range.^[39,41,59] Because of its unique properties of remote control and ultrafast on-demand nanoscale thermal production, it has also been widely employed in biosensing and manipulation of cellular functions, such as ultrafast plasmonic PCR,^[60–62] intracellular gene delivery and release,^[63] as well as single-cell neural activity control.^[64–68]

The above three optofluidic applications are greatly influenced by optical and thermodynamic interactions. By carefully tailoring these interactions, one can achieve their desired optofluidic functions. In this review, in Section 2, we first examine plasmonic optothermal generation from a theoretical perspective, then present a series of hydrodynamic phenomenon related to the nanoscale temperature gradient generation, such as theoretical models of natural convection, the Marangoni effect, thermophoresis, and other thermodynamic effect. In Section 3, state-of-the-art thermal optofluidic applications on the nanoscale are described in detail. Finally, in Section 4, challenges and future opportunities of thermal optofluidics are discussed.

2. Operational Principles

2.1. Origin of Heat in Thermal Optofluidics: Plasmonic Thermal Effect

The underlying physics of the plasmonic thermal effect can be simplified as follows: when a metallic (gold, silver, or other noble metal) nanostructure is excited at its plasmonic resonant frequency ω ,^[12] the electric current $\mathbf{J}(\mathbf{r})$ (the complex amplitude of the electronic current density inside the nanostructure) originating from the electronic oscillations inside the metal is damped by lattice resistance. In this way, the incident light energy is transformed into thermal energy, termed the Joule heating effect. In a nanostructure with a nonuniform shape excited by a plane wave, the thermal generation is derived from the heat power density $q(\mathbf{r})$ (power per unit volume) inside the nanostructure, and the total power absorbed is expressed as $Q = \int_V q(\mathbf{r}) d^3r$, where the integral covers the entire nanostructure volume V . Because the heat originates from Joule effects, the heat power density is^[69]

$$q(\mathbf{r}) = \frac{1}{2} \text{Re}[\mathbf{J}^*(\mathbf{r}) \cdot \mathbf{E}(\mathbf{r})] \quad (1)$$

where ϵ_0 is vacuum permittivity, $\epsilon(\omega)$ is the relevant permittivity of the nanostructure, $\mathbf{E}(\mathbf{r})$ is the electrical field, $\mathbf{J}(\mathbf{r}) = i\omega\mathbf{P}$ and the electric polarizability $\mathbf{P} = \epsilon_0\epsilon(\omega)\mathbf{E}$, so that

$$q(\mathbf{r}) = \frac{\omega}{2} \text{Im}(\epsilon(\omega))\epsilon_0|\mathbf{E}(\mathbf{r})|^2 \quad (2)$$

Therefore, the thermal power inside the nanostructure is proportional to the square of the excitation electric field. If the absorption cross section σ_{abs} of the nanostructure^[70] is known, the total power can be simplified as: $Q = \sigma_{\text{abs}}I$, where I is the irradiance of the excitation light (power per unit area).

Upon irradiation, the thermal transportation process happens within nanoseconds, and the nanostructure begins to heat up immediately. Note that the traditional Fourier heat conduction theory is no longer valid for heat transportation in the vicinity of nanoparticles with sizes smaller than the mean free

path of the heat carrier. As a result, the temperature is higher inside the nanoparticle and the heat carrier transportation is nonlocal, which implies that there is a temperature jump because of the discontinuity of heat conduction.^[71] Therefore, these optically induced thermal converters can create strong or abrupt thermal gradients in the microfluidic system.

In addition, the typical measurement method of nanoscale temperature distribution is utilizing the temperature-dependent fluorescent dye, such as rhodamine B.^[43,72,73] The temperature in microscale can be calculated from the fluorescent intensity after the calibration curve about fluorescent intensity versus temperature is obtained. While the temperature measurement of microfluidic devices is still an ongoing topic, other methods such as ultrasonic method,^[74] micron-resolution particle Brownian motion detection method,^[75] fluorescence lifetime thermal imaging,^[76,77] etc. have been developed for better measurement resolution and dynamic range.

2.2. Natural Convection

If the aforementioned metallic nanostructure is placed at the bottom of the microfluidic chamber, some form of thermal diffusion process will be activated upon excitation by a plane wave $\mathbf{E}(\mathbf{r})$. Baffou et al. performed a comprehensive study on the heat generation of plasmonic nanostructures. Their results indicate that $q(\mathbf{r})$ inside a nanostructure depends on its structural morphology, and can be highly non-uniform.^[14,78,79] Thus, the influence of the temperature distribution $T(\mathbf{r}, t)$ inside the nanostructure is governed by the heat-conduction equation

$$\rho_m c_m \frac{\partial}{\partial t} T(\mathbf{r}, t) - \kappa_m \nabla^2 T(\mathbf{r}, t) = q(\mathbf{r}) \quad (3)$$

where ρ_m is the metal's density, c_m is the metal's specific heat capacity at constant pressure, and κ_m is the thermal conductivity of the metal. Despite the nonuniform $T(\mathbf{r}, t)$ inside the nanostructure, the temperature throughout the structure is homogeneous because of the high thermal conductivity of the metal in comparison to water. If there is no heat source outside the structure, $q(\mathbf{r}) = 0$, but natural convection may occur. The temperature distribution in the surrounding fluid is governed by

$$\rho_s c_s \left[\frac{\partial}{\partial t} T(\mathbf{r}, t) + \nabla \cdot (T(\mathbf{r}, t) \mathbf{v}(\mathbf{r}, t)) \right] - \kappa_s \nabla^2 T(\mathbf{r}, t) = 0 \quad (4)$$

where $\mathbf{v}(\mathbf{r}, t)$ is the surrounding fluid velocity and $\nabla \cdot (T(\mathbf{r}, t) \mathbf{v}(\mathbf{r}, t))$ is a convective term. κ_s is the thermal conductivity of water, ρ_s is the density of water, and c_s is the specific heat capacity of water at constant pressure.

The water density surrounding the metal nanostructure will decrease as the temperature of the nanostructure rises, thus generating an upward convective flow. Due to fluidic continuity, the fluid in other locations will flow toward the center of mass reduction in a toroidal shape. The Navier–Stokes equation describes this profile of the fluid velocity

$$\frac{\partial}{\partial t} \mathbf{v}(\mathbf{r}, t) + (\mathbf{v}(\mathbf{r}, t) \cdot \nabla) \mathbf{v}(\mathbf{r}, t) = \nu_s \nabla^2 \mathbf{v}(\mathbf{r}, t) + \mathbf{f}_t(T(\mathbf{r}, t)) \quad (5)$$

where ν_s is the surrounding fluid viscosity and \mathbf{f}_t is the force per unit mass due to the temperature gradient. To reduce the computational complexity when solving nonisothermal flow problems, Boussinesq approximation is usually implemented, which implies that the flow density variation is only important in the term \mathbf{f}_t , and have no effect in other terms. Typically, in natural convection, \mathbf{f}_t is temperature-dependent buoyancy force, one can estimate \mathbf{f}_t as^[80]

$$\mathbf{f}_t(T) = \beta_s g(T(\mathbf{r}, t) - T_0) \mathbf{z} \quad (6)$$

where β_s is the dilatation coefficient of the fluid, g is the gravitational acceleration, T_0 is the initial temperature, and \mathbf{z} is the upward z -direction unit vector. In the example shown in **Figure 1**, the convective flow is known as a Rayleigh–Benard fluid convection or natural convection (buoyancy convection), and the time taken to reach a steady state (nano- to microseconds) depends on the size of the nanostructure, and it can be suppressed by shorten the chamber height in the z direction.^[17]

Therefore, the surrounding water can be modeled by Equations (3) to (6) when considering thermally induced natural fluid convection and the temperature distribution at the microscale. For more detail, refer to Donner et al. and Baffou et al.,^[14,17,78,79] whose well-rounded studies of this problem provide good guidance for understanding the nanoscale convection induced by plasmonic structures. In addition, as for the measurement of fluidic velocities in practical experiments,

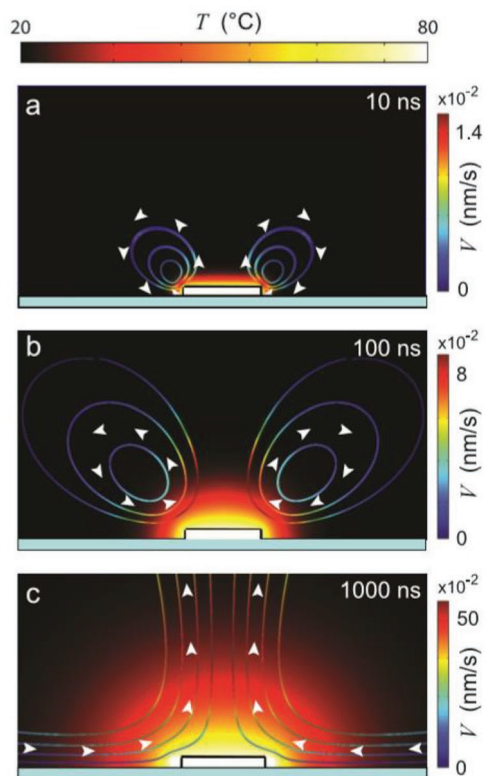


Figure 1. Simulation of fluid convection around a gold nanodisk with a height of 40 nm and diameter of 500 nm in water; the disk is heated at time $t = 0$ from room temperature to 80 °C. a–c) The temperature and velocity distribution at different times. Reproduced with permission.^[17] Copyright 2011, American Chemical Society.

usually microsize tracing particles are added into the fluidics for flow visualization. This is a well-developed method called Particle Image Velocimetry (PIV).^[81]

2.3. Marangoni Convection

Compared with the natural convection described above, Marangoni convection is a much stronger convective flow,^[18] which commonly occurs at liquid–gas interfaces under comparable thermal energy inputs. While natural convection originates from fluidic gravity induced by the temperature-dependent density of the fluid, Marangoni convection is caused by the temperature-dependent surface tension at the liquid–air interface, where the fluid molecules are dragged toward regions with higher surface tension,^[82] so it is also called thermocapillary effect. In most cases, liquid surface tension decreases linearly with increasing temperature. Thus, an interfacial shear stress τ_s is generated, oriented from the hot to the cold side, and it is inversely proportional to the temperature gradient ∇T

$$\tau_s = -\sigma_T \nabla T \quad (7)$$

where σ_T is the temperature coefficient of surface tension, which can be calculated according to the Eötvös law.^[83]

Moreover, as shown in **Figure 2**, to retain fluid continuity, the tangential surface velocity u_s is directed toward the cold region near the liquid–air interface and then flows back to the hot side via subsurface flow. The depth of this circulating cell depends on the length and depth scale of the flow in the chamber.

In addition, a recent study of Marangoni convection revealed that the solute component can greatly influence the convection, and the solute concentration gradient along the liquid–air interface can influence the surface tension just as the temperature gradient does.^[20] Therefore, both the thermal-Marangoni and solute-Marangoni effects must be taken into consideration when dealing with the corresponding applications.

2.4. Thermophoresis

Thermophoresis is an interfacial phenomenon caused by thermal gradient-induced particle–solvent interface

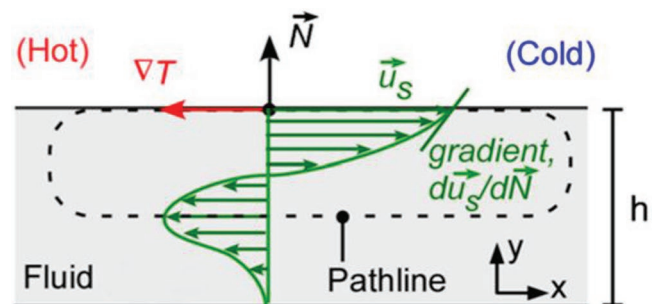


Figure 2. Schematic of cross section of Marangoni flow driven by a surface temperature gradient, where ∇T , u_s , and \mathbf{N} refer to surface temperature gradient, tangential surface velocity, and the surface normal vector, respectively. The parallel flow vectors illustrate the typical profile of surface and subsurface flow. Reproduced with permission.^[19] Copyright 2008, IOP Publishing.

inhomogeneity.^[84] When a small particle or solvent molecule encounters a temperature gradient, thermal diffusion ensues, with a thermophoretic force being exerted on the particle along the temperature gradient toward either the hot side or the cold side. Under a temperature gradient ∇T , the total mass flux is

$$J = -D\nabla c - cD_T\nabla T \quad (8)$$

where D is the Brownian diffusion coefficient, D_T is the thermal diffusion coefficient or thermophoretic mobility, and c is the concentration of the particles. In the absence of convection, a steady-state concentration gradient can be obtained as

$$\nabla c = -cS_T\nabla T \quad (9)$$

The particle drift velocity is given by

$$v_T = -D_T\nabla T \quad (10)$$

where $S_T = D_T/D$ is the Soret coefficient. According to Equation (9), when the sign of S_T is positive, particles are transported to the cold side, and the colloidal system is termed thermophobic. Conversely, when the sign is negative, particles are transported to the hot side, and the colloidal system is termed thermophilic. The measurement and origin of thermophoresis are still topics of broad investigation.^[85–87] Currently, it is commonly believed that the magnitude and sign of the Soret coefficient S_T are susceptible to the influence of particle size,^[88] surrounding temperature,^[22] Debye length,^[87] ion concentration, and pH value.^[89–91] Several elemental phenomena have been invoked to explain the origin of thermophoresis, such as effects driven by the interfacial tension gradient,^[92] van der Waals forces,^[93] the electrolyte Seebeck effect,^[91,94] and surface entropy contributions.^[48,87]

2.5. Electrolyte Seebeck Effect

In an electrolyte solution, the direction and magnitude of the thermophoretic force can be greatly influenced by the electrolyte, especially for charged colloidal particles, as the electrolytes are themselves subjected to thermophoresis. Thermophoresis of the electrolytes can lead to a nonuniform electrical field, which in turn influences the motion of the colloidal particles. Within a finite spatial region, the ion diffusion can ultimately reach a steady state, in which the charge accumulates in a thin layer of Debye length (λ_{DH}) near the microfluidic boundaries. Thus, the spatial separation between the anions and the cations creates an electric field, which is known as the electrolyte Seebeck effect.^[91,95,96] The induced electric field

$$E = S_s \nabla T \quad (11)$$

is proportional to the Seebeck coefficient S_s and the temperature gradient.^[97] This phenomenon is analogous to the well-understood Seebeck effect in semiconductors, which applies in a thermocouple. It is induced by the thermophoresis of electrolyte ions while the solvent retains overall charge neutrality. Note that due to the setting-up of the electrolyte concentration gradient, the osmotic pressure will counteract the thermophoretic force, thus reducing the Seebeck effect.

An example of the Seebeck effect is the stronger tendency of OH^- ions to accumulate at the cold side after NaOH is added

to an aqueous suspension of negatively charged particles. This occurs because the S_T of the OH^- anions is larger than that of the Na^+ cations, which generates a steady-state electric field pushing the suspended negatively charged particles to the hot side.^[98] Figure 3 shows the Soret coefficient of 215 nm polystyrene beads in a 1×10^{-3} M solution of $\text{NaCl}_{1-x}\text{OH}_x$ as a function of the composition parameter x . The data show a linear variation with x ; at 41 °C the values change signs at $x = 0.5$. These findings are in agreement with previous studies reporting that $S_T(\text{particle}) > 0$ in NaCl, while $S_T(\text{particle}) < 0$ in NaOH, with the Soret coefficients of the three ions being in the order $S_T(\text{OH}^-) > S_T(\text{Na}^+) > S_T(\text{Cl}^-)$.^[89,91,95]

2.6. Depletion Force

In semiconductors, a depletion region is induced by the charge carriers' concentration gradient. Analogously, in a hybrid colloidal-molecular system in which the molecules in the solvent are much smaller than the colloidal particles, the molecules drift from the hot to the cold region when they are subjected to thermophoresis under a temperature gradient. This creates a concentration gradient ∇c , which gives rise to an osmotic pressure proportional to ∇c , which tends to push the particles from the low- to the high-temperature region. Such depletion forces have been studied extensively as a means of controlling the trapping and assembling of colloidal particles by tailoring the characteristics of the depletant molecules or nanoparticles.^[25,26,99,100]

2.7. Interfacial Effect in Colloidal Particles

In addition to electrolytes in solution, the interfacial effect of colloidal particles is another necessary consideration in

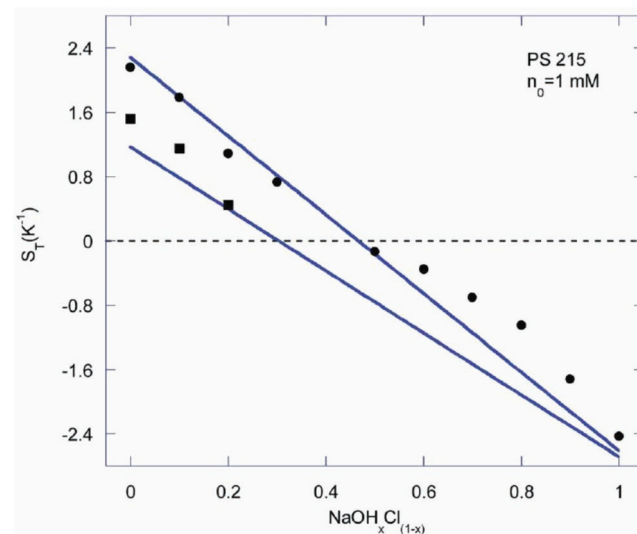


Figure 3. Soret coefficient of 215 nm polystyrene (PS) beads in the mixed electrolyte $\text{NaCl}_{1-x}\text{OH}_x$. The data at 41 °C (circles) show a linear dependence on x and a change of sign at $x = 0.5$; those at 26 °C (squares) indicate that in NaCl solution, S_T strongly increases with temperature. Reproduced with permission.^[90] Copyright 2013, Royal Society of Chemistry.

optofluidic manipulation. At the interface between two phases, typically liquid–solid or liquid–air, there exist two parallel layers of opposite charges. The inner layer close to the surface comes from the self-charge of the surface or ions adsorbed onto the surface due to chemical bonding. The outer layer, composed of ions, is loosely attracted to the surface charge via Coulomb force. The outer layer in the liquid phase can be further divided into two layers, usually termed an electric-double-layer (EDL). Since the first and simplest EDL model formulated by Helmholtz in 1879,^[29] many attempts have been made to describe the phenomenon, such as the Gouy–Chapman^[28,101] and Stern models.^[27] Measurements of surface tension and interfacial capacitance also provide information about the EDL. The voltage drop across the EDL is called the zeta potential,^[102] and is a crucial factor in the behavior of a colloidal particle. The zeta potential depends on various colloidal particle properties, such as particle size, surrounding temperature, and colloidal ion concentration, which are also key factors influencing thermophoresis. It was recently reported that the optical force can also influence the EDL by affecting the particles' polarizability.^[103] Therefore, one should take the EDL and its zeta potential into account when modeling the behavior of colloidal particles in optofluidic manipulation experiments.

2.8. Other Interactions

In addition to the phenomena mentioned above, other optical interactions including scattering forces, gradient force, and photophoretic force^[104,105] play important roles in optofluidics. Other interactions such as gravity, optofluidic nonlinear effects,^[106] and particle–particle interaction^[107,108] should also be taken into consideration when dealing with specific thermal optofluidic applications. Interested readers may refer to other reviews for further details of these interactions.^[31,109]

3. Thermal Optofluidic Applications

3.1. Manipulation of Colloidal Particles

3.1.1. Natural Convection and Thermophoresis-Induced Tweezers on Gold Nanoislands

In 2015, we performed the first optothermal trapping and assembling of microsized particles and live cells on a substrate of gold nanoislands (Au-NIs), in which the substrate's surface morphology and optical absorption were readily tunable by a simple annealing process to facilitate its practical fabrication.^[54] As shown in **Figure 4a**, when a laser is focused on the surface of Au-NIs with a colloidal solution of polystyrene (PS) spheres immersed above the substrate, the PS particles are trapped and assembled into a low 3D conical shape at the focusing spot. Besides an Au-NI substrate on a planar surface, an Au-NI-coated single-mode fiber tip also has a good trapping ability, as shown in **Figure 4d,e**. The illustration in **Figure 4b** shows that the trapping phenomenon is a combined effect of optical gradient force, thermophoresis, and natural convection induced by the Au-NIs. First, the lateral convective flow drags the PS

particles near the substrate surface toward the hot center via a Stokes force $\mathbf{F} = \mu\mathbf{v}$, where $\mu = 3\pi\eta\epsilon D$ is the drag coefficient, with the dynamic viscosity of fluid η , particle diameter D , particle velocity v , and ϵ is a correction factor accounting for the particle's proximity to the substrate.^[110,111] Then, when the particles arrive at the hot region, the thermophoretic force with negative S_T and the near-field optical force both clamp and trap the PS particles at the hot region.

In our experiments, a negative S_T was obtained, and under the resulting temperature gradient, colloidal particles were driven to the hot region. To explain this phenomenon, we invoked the interfacial entropy gradient induced thermophoresis.^[48,87] The colloidal particles used in our system had negative charges on the surface, with zeta potentials ranging from -20 to -40 mV. These charges polarized water molecules and electrostatically attracted them to the particles' surface, generating a tightly bound Helmholtz plane, followed by a loosely bound Gouy plane. According to Anderson's theory, which accounts for the colloidal particle slip velocity and boundary conditions,^[112] at a distance r from the particle surface, the enthalpy increment from the solid–liquid interface is

$$h(r) = 1/2(\epsilon + T \partial\epsilon/\partial T)E^2(r) \quad (12)$$

where ϵ is the relative permittivity of water, $E(r) = \kappa\zeta\exp(-\kappa r)$ denotes the electric field, in which κ^{-1} is the Debye length and ζ is the zeta potential. In this case, the thermal diffusion coefficient (thermophoretic mobility) is

$$D_T = -\frac{2}{\eta T} \left[\frac{2\Lambda_1}{2\Lambda_1 + \Lambda_p} \right] \int_0^\infty rh(r)dr = -\frac{1}{4} \cdot \frac{\zeta^2}{\eta T} \left[\frac{2\Lambda_1}{2\Lambda_1 + \Lambda_p} \right] \left(\epsilon + T \frac{\partial\epsilon}{\partial T} \right) \quad (13)$$

where η , Λ_1 , and Λ_p are the viscosity of water and the thermal conductivity of water and particle, respectively. Within a temperature gradient field, a permittivity imbalance occurs along ∇T at the EDL. Under such conditions, at room temperature, the value of the term $\left(\epsilon + T \frac{\partial\epsilon}{\partial T} \right)$ becomes positive at the EDL

while it is negative in bulk water.^[113] Thus, the D_T surrounding the particles is negative, so the particles are driven from the cold to the hot region. Because this trapping scheme is assisted by plasmonic thermal effects, it has several advantages over traditional optical trapping, such as lower power consumption and longer-range particle transportation. The laser power densities used range from 8.8 to 128.2 mW mm⁻², much lower than for traditional optical tweezers. This tool enables micro- and nanoobject manipulation for applications in disciplines such as biomedical engineering, physics, and chemistry. Moreover, the fiber-based trapping scheme is readily integrated with other optical systems to extend the manipulation from 2D to 3D. Recently, thermophoresis-induced optical manipulation and assembling techniques have been extensively studied by Zheng and co-workers via particle surface modification and surface entropy tuning.^[46–48]

To further explore the utility of plasmonic heating-induced tweezers and avoid interference by optical forces, we investigated the effects of an optics-free microscale electric thermal heater (METH) on a continuous gold thin film via femtosecond laser writing and photolithography.^[43,114] Upon applying a

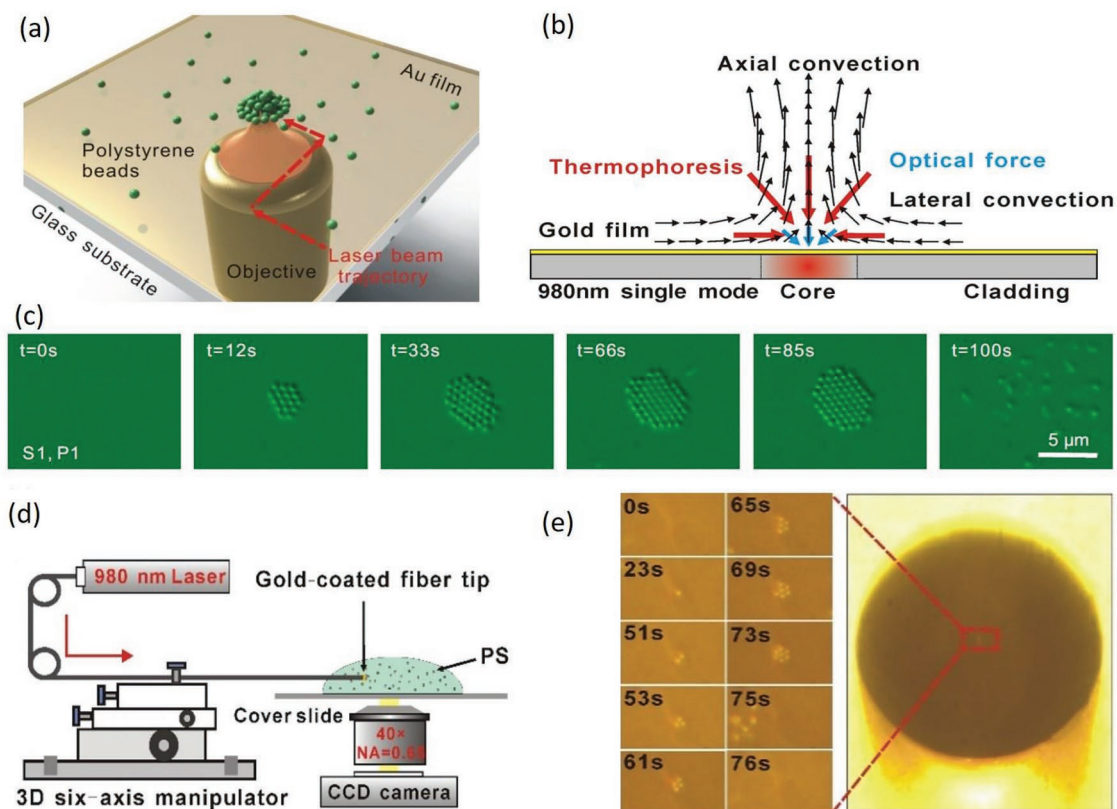


Figure 4. a) Optical setup of our trapping experiments. b) Different force components in the trapping experiment. The force components due to thermophoresis, convective flow, and optical gradient are represented by arrows in red, black, and blue, respectively. The central hot region can be established by light irradiation from the fiber core or a focused laser beam. c) Successive image frames showing the trapping of polystyrene particles (500 nm in diameter) at a laser power of 1.0 mW. d) Experimental setup of optical trapping on gold-coated fiber tip. e) Results of the trapping 1 μm polystyrene beads on the gold-coated fiber tip, after the 980 nm laser excitation was switched on at 0 s, the polystyrene beads around the fiber tip are gradually trapping to fiber core area. Immediately after switching off the laser at 75 s, the trapped beads are released to the surrounding solution. b,d,e) Reproduced with permission.^[41] Copyright 2015, The Optical Society. c) Reproduced under the terms of the Creative Commons Attribution 4.0 International License.^[39] Copyright 2015, Springer Nature.

voltage across the structure, a micro-sized heater similar to a laser-focus heating spot is created, in which the temperature gradient-induced thermal convection and thermophoresis are able to trap and assemble the particles into the hot micro-sized area. Moreover, as the experiments shown in **Figure 5**, we designed different METH structures to achieve particle trapping, sorting, and assembling. Because the temperature gradient profile is identical in shape to the METH structure, and the trapping effect is dominated by thermophoresis, the trapping area takes the shape of the METH structure. With the advantages of an optic-free mechanism, METH trapping approaches can be integrated with various types of optic-free microfluidic platform as well as lab-on-a-chip systems to make the systems more compact and versatile.

3.1.2. Optothermoelectric Nanotweezers

Using a customized particle-surface modification process, Lin et al. recently developed optothermoelectric nanotweezers, which exploit the electrolyte Seebeck effect to manipulate metallic particles.^[47] A cationic surfactant,

cetyltrimethylammonium chloride (CTAC), was used to modify the particle surfaces. As shown in **Figure 6a,b**, the CTAC-coated metallic particles obtained a positive surface charge. When the concentration of CTAC was just slightly above the critical micelle concentration ($0.13\text{--}0.16 \times 10^{-3} \text{ M}$), the molecules assembled into spherical positive micellar ions (positive ion clusters), resulting in a solution of Cl^- anions and CTAC micellar cations. Under a laser beam-induced temperature gradient, the thermophoresis of both ionic species will push them toward the cold region. However, because the Soret coefficient of the micellar ions is larger than that of the Cl^- ions, there is a spatial displacement between the two ionic species and a thermoelectric field is generated, pointing toward the hot region. Therefore, as shown in **Figure 6d,e**, the positively charged metallic particles are driven to and trapped in the hot region.

3.1.3. Natural Convection-Induced Trapping and Assembling of Particles

It is possible to optically induce the trapping and assembling of colloidal metal nanoparticles solely by using natural

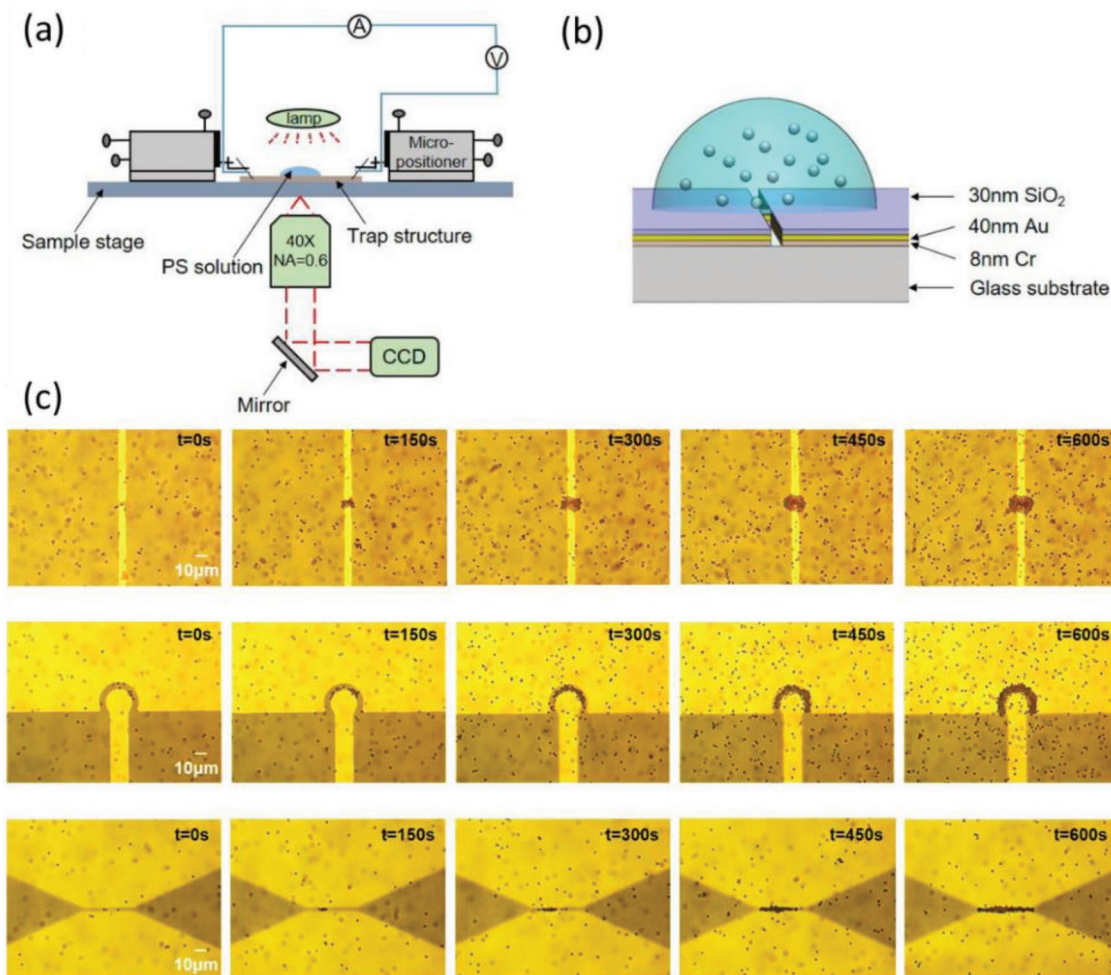


Figure 5. a,b) Experimental setup and a single METH structure. c) Trapping of 1.5 μm colloidal particles on narrow slit, annular ring, and long wire bridge. Reproduced with permission.^[43] Copyright 2018, Elsevier.

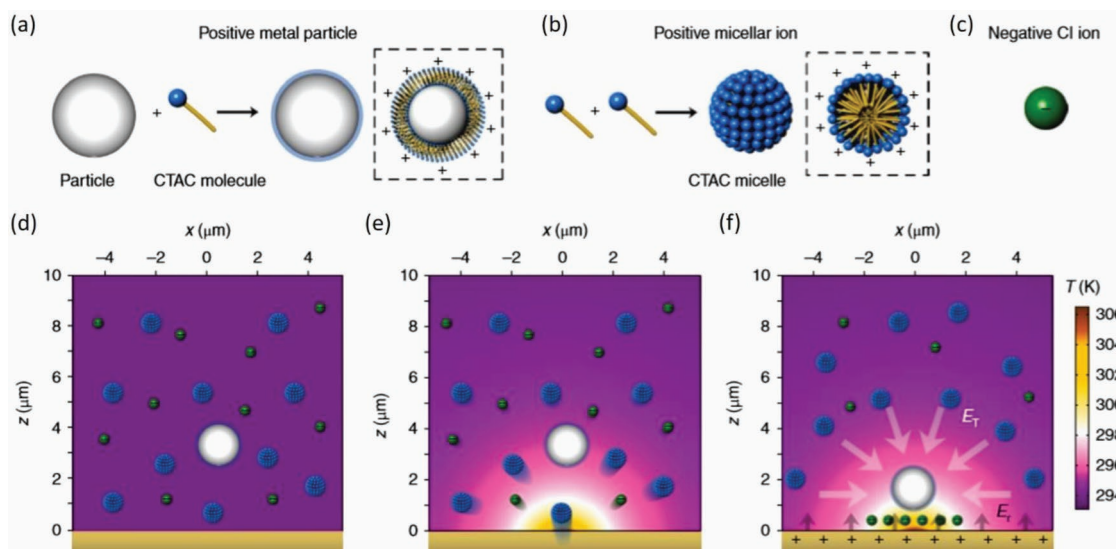


Figure 6. a–c) Schematic view of positive charge modification on metal nanoparticle surface by CTAC molecule, CTAC micelle formation, and Cl^- ion. d–f) Schematic illustration of the trapping effect. Under a temperature gradient, ion thermophoresis induces the displacement of negative Cl^- ions and positive micellar ions; a thermoelectric field is thus formed in the direction of the hot side, which pushes the positively charged particles to the hot center and traps them there. Reproduced with permission.^[47] Copyright 2018, Springer Nature.

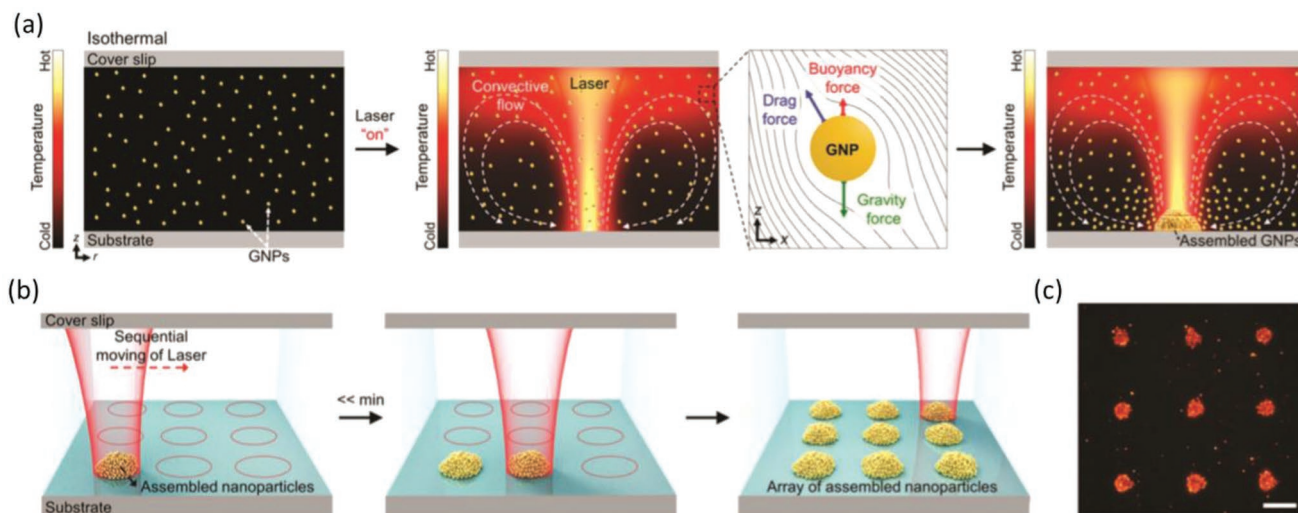


Figure 7. a) Schematic of the working principles of convection-induced particle assembly. b) Photothermal convection lithography of assembled patterned colloidal array. c) Dark-field imaging of assembled gold nanorod array. Scale bar = 100 μm . Reproduced with permission.^[115] Copyright 2018, Wiley-VCH.

thermal convection. Recently, Jin et al. successfully assembled metal nanoparticles via thermal convection without the need for chemical ligand bonding or a thermally absorptive substrate.^[115] As shown in **Figure 7**, they utilized the optothermal response of suspended gold nanoparticles to create a convective flow, and the flow in turn dragged the particles along the streamlines into the laser-focus plane on the bottom substrate, where the nanoparticles assembled together via van der Waals forces. The process can be completed within 1 min and the assembly size can be tuned by the duration of laser illumination. This rapid particle trapping and assembling technique has several advantages, such as obviating the need for a thermally absorptive substrate and enabling the assembly of a patterned array.

3.1.4. Marangoni Convection-Induced Particle Manipulation

Marangoni convection originates from the surface tension imbalance caused by a temperature gradient, as mentioned in Section 2. This effect operates near the interface of different phases and drives the particles along a temperature gradient from the cold to the hot region. The manipulation of colloidal particles based on interfacial Marangoni convection has been reported.^[18] As **Figure 8** shows, a 55 wt% solution of polyethyleneglycol (PEG) with high viscosity compared with water is used to suppress the particles' Brownian motion in the experiments. Thus, an air-PEG interface serves as the medium for manipulating the gold particles in the colloidal solution. Upon near-infrared (NIR) laser illumination at the air-PEG liquid interface, a local temperature gradient is established and Marangoni convection drives the 80 nm gold nanoparticles to flow in the direction of the green arrows shown in **Figure 8a**. It is worth noting that the temperature increment is only 1.75 K when using a laser power of 60 mW in this system due to the low optical thermal absorptivity of the PEG solution.

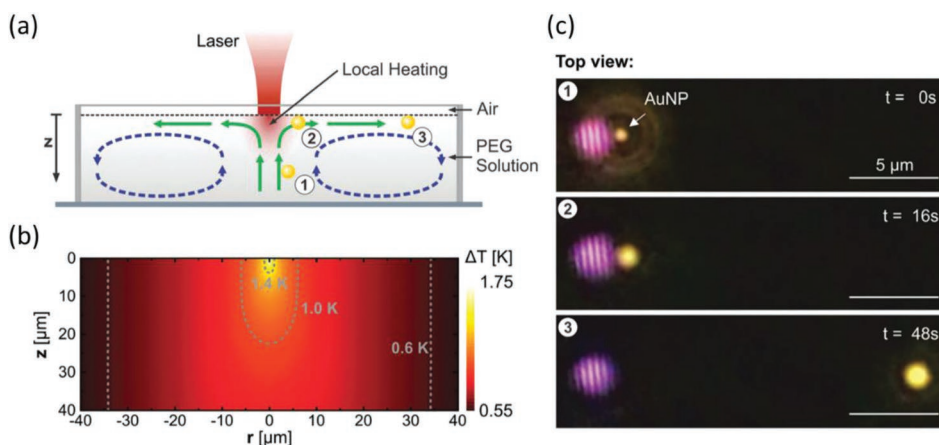


Figure 8. a) Schematic of nanoparticle manipulation by Marangoni convection. The green arrows denote Marangoni convection and the blue arrows denote natural convection. b) Estimated temperature profile at 60 mW laser power illumination. c) A single gold nanoparticle (AuNP) being transported from position 1 to position 3 (positions shown in (a)). Reproduced with permission.^[18] Copyright 2018, Royal Society of Chemistry.

Following the aforementioned particle manipulation scheme, more recently, Lv et al. developed light-actuated Marangoni tweezers.^[58] Instead of relying on a temperature-induced surface tension gradient, this method uses a photoswitchable surfactant with two isomeric states, *trans* and *cis*, to create a surface tension imbalance. As shown in **Figure 9**, the

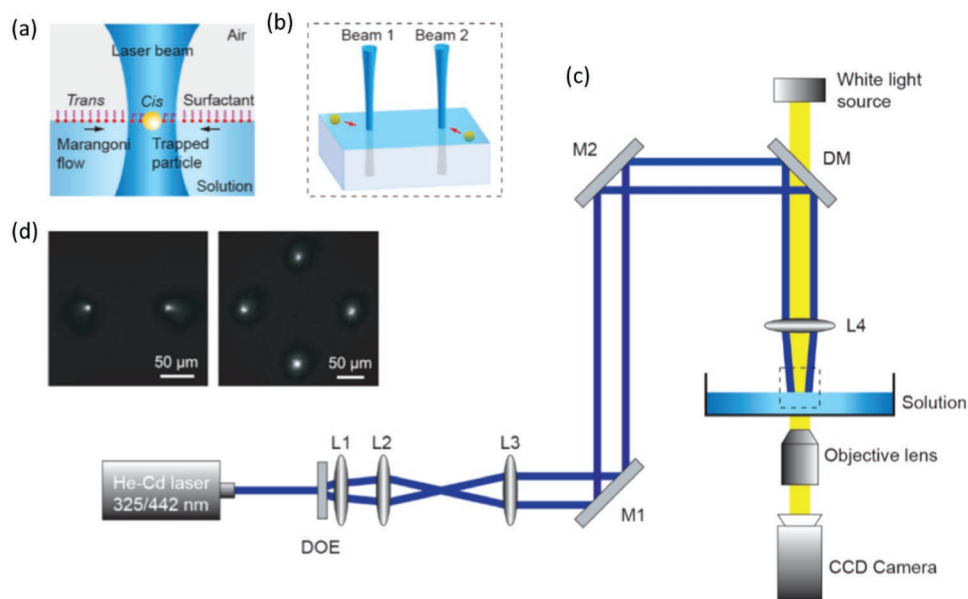


Figure 9. a,b) Working principle and c) experimental setup of light-actuated Marangoni tweezers. d) Experimental results under microscopy: Two and four particles are trapped under patterned illuminations. Reproduced with permission.^[58] Copyright 2018, American Chemical Society.

gold nanoparticles at the air–solution interface can be precisely trapped at the laser focusing region, whereupon the surfactant *cis* state is turned on. These emerging tools of Marangoni convection-induced particle manipulation have opened up new methods via designing various types of interface for controlling more complex nanoparticle movements.

3.2. Optofluidic Actuation Techniques

3.2.1. Optofluidic Applications Based on Gold Nanoislands

In the previous section, we introduced the use of Au-NIs to produce thermal convection and thermophoresis-induced tweezers. The highly efficient conversion of optical power to hydrodynamic actuation by Au-NIs also greatly facilitates applications in optofluidic actuation.^[53] In 2015, we achieved optically induced flow guiding, valving, and mixing hosting on one substrate.^[54]

Figure 10a illustrates the method for optofluidic guiding. First, PDMS microfluidic channels are fabricated for hosting the fluidic motion. When a laser spot is focused at the meniscus region, a small amount of water is evaporated because of thermal generation in the Au-NIs. Then, the vapor immediately condenses into droplets in front of the meniscus. The droplets grow larger as more water vaporizes, and within a short period, the droplet in front is large enough to coalesce with the bulk water behind and form a new continuous water column. Therefore, the water boundary advances one step forward. This sequence of steps continues, as the laser spot's moving speed is slow enough for the droplets to grow and coalesce. Therefore, one can direct the fluidic motion in any direction inside the channel via laser focusing.

Elsewhere, optofluidic valving was achieved by utilizing the heating-induced fluidic motion of the Au-NIs. As illustrated in

Figure 10b, an Au-NIs strip is coated on the narrowing region of a microfluidic channel to serve as the optothermal responsive valve. Before the excitation laser is switched on, the narrowing region creates a constant counter-pressure originating from the surface tension of the liquid-front meniscus, thus blocking the fluid in the upper channel from flowing through. After the laser is switched on, the optothermal generation of Au-NIs pushes forward the liquid-front meniscus, which weakens the counter pressure. When the counter pressure is less than the downward pressure P_w , the liquid in the upper channel can flow through. Additionally, an optofluidic thermally induced microbubble stirrer is created above the Au-NIs, as shown in **Figure 10c**. Once the laser is focused on the liquid–air interface of the bubble, a Marangoni flow is generated to perform microfluidic mixing at any location of interest. Therefore, the use of a random plasmonic substrate (namely, Au-NIs) to address the three challenges of low-Reynolds-number optofluidic actuation systems mentioned in the Introduction is promising for multiple fluidic control and in situ detection of solution-based reactions.

3.2.2. Optothermally Induced Microbubbles for Optofluidic Actuation

Optothermally induced microbubbles are widely used as actuators in optofluidic systems for their abilities to generate strong microscale Marangoni convection and rapid optocontrolled size variation. Their applications include cavitation bubbles to perform microfluidic pumping,^[116,117] optofluidic switching via bubble-induced microfluidic channel squeezing,^[118] light-controlled microvalves in the microfluidic channel,^[119] and bubble-induced micropattern fabrication.^[120] Despite the wide variety of microbubble-based optofluidic applications that have been demonstrated,

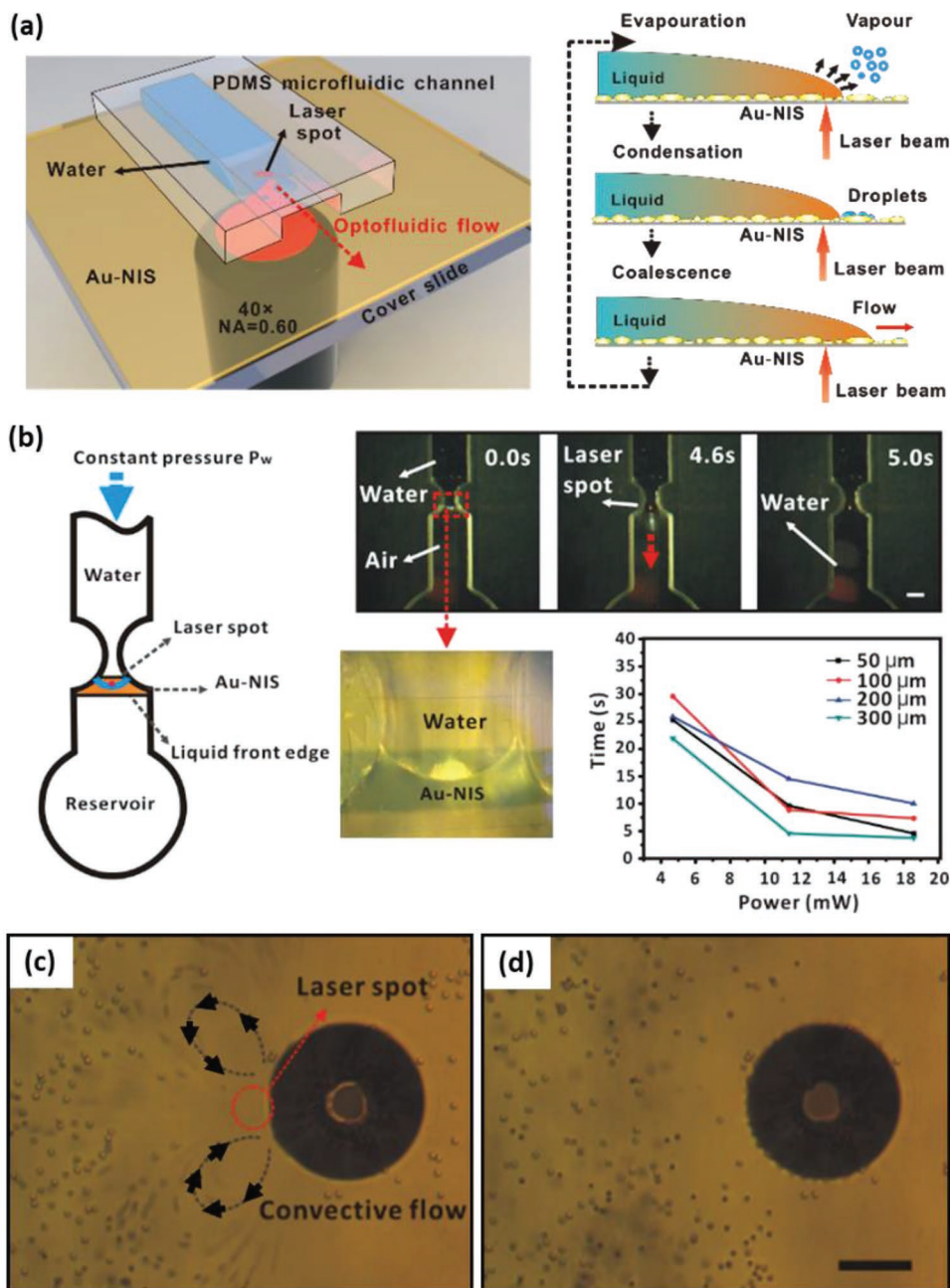


Figure 10. a) Optical setup and working principles of optofluidic guiding. b) Schematic and temporal sequence of the optofluidic valve, where the Au-NIS strip width is 150 μm and the scale bar denotes 500 μm . The graph shows the relationship between valve opening time and laser power for different valve widths (from 50 to 300 μm). c) Optofluidic bubble stirrer: a 785 nm laser (12 mW) was used to sustain a stable Marangoni convective flow at the liquid–air interface. d) No convective flow was observed after the laser was switched off. Scale bar = 40 μm . Reproduced with permission.^[54] Copyright 2015, Royal Society of Chemistry.

mechanistic studies of the microbubbles' effects are still at an early stage. Some studies have shown that the direction, convective flow range, and magnitude of the optothermally induced Marangoni effect around a water vapor microbubble can be tuned by the solute components^[20] and the water degassing process.^[121] These mechanistic studies provide a good foundation for the design of microbubble-assisted optofluidic systems.

3.2.3. Optothermally Induced Convection Flow for Optofluidic Manipulation

Recently, Zheng et al. developed an optofluidic manipulation technique by controlling the natural and Marangoni convection via optothermal generation on hybrid photothermal waveguides.^[122] As shown in **Figure 11**, the thermal source of the system is based on a coated layer of graphene oxide (GO)

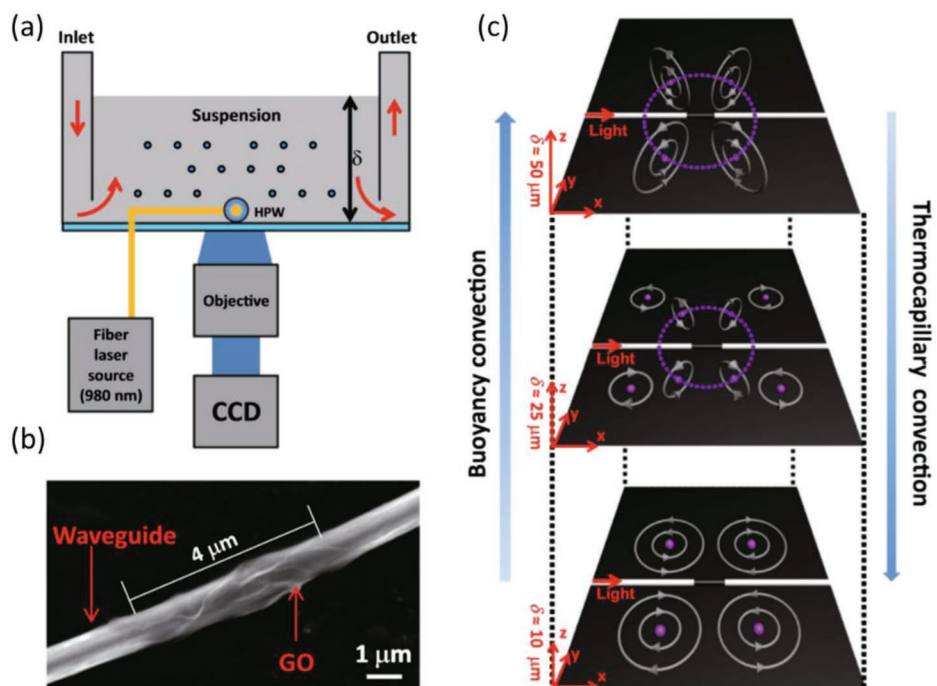


Figure 11. a) Schematic of the setup for buoyancy and thermocapillary convection. b) SEM image of graphene oxide-coated hybrid photothermal waveguide. c) The relative contribution of the two forms of convection is tuned by the fluid thickness δ . Reproduced under the terms of the Creative Commons Attribution 4.0 International license.^[122] Copyright 2018, The Author(s). Published by Springer Nature.

on a SiO_2 waveguide. Owing to the high infrared absorptivity and thermal conductivity of the GO coating, upon excitation by a 980 nm laser, vertical convection inside the fluid (buoyancy convection) and horizontal convection inside the vortices (thermocapillary convection) close to the fluid interface are generated simultaneously in three dimensions around the waveguide. Because thinner microfluidic chamber thickness can suppress the buoyancy convection^[17] and enforce the thermocapillary convection since the water–air interface is closer to heat source,^[122] the transition from buoyancy to thermocapillary convection can be achieved by tuning the fluid thickness δ . With the ability to switch between the two optofluidic modes, this approach can be applied in high-throughput systems for optofluidic arrangement and mixing.

3.3. Thermal Optofluidics in Biological Applications

3.3.1. Optothermal Nucleic Acid Amplification

The polymerase chain reaction (PCR), invented in the 1960s, is a ubiquitous and an essential tool for biological research. PCR is used to amplify nucleic acid markers via a polymerase reaction from a primer-bound region under thermocycling conditions, which involves denaturation, annealing, and elongation of the target nucleic acid marker. Developing a simple and robust PCR thermal cyler for rapid on-site genetic screening remains challenging for point-of-care-testing. Prior to the availability of plasmonic PCR, a droplet-based real-time PCR system with photothermal heating was reported in which direct

absorption of a 1480 nm IR laser beam for laser-assisted heating by water droplets enables high-speed thermocycling with a switching time of 0.8 s at between 60 °C and 95 °C.^[116]

As mentioned in Section 2, plasmonic nanostructures enable ultrafast localized photothermal light-to-heat conversion, which provides an advanced method of ultrafast thermocycling. One of the characteristics of photothermal conversion is wavelength dependence, which makes this method capable of accurately tuning the temperature by varying the laser wavelength in addition to the illumination power and duration. Plasmonic PCR can be performed either on a plasmonic surface or in a suspension of nanoparticles. Plasmonic PCR was first demonstrated in 2012 in the amplification of human androgen receptor DNA, where citrate-capped gold nanoparticles were mixed with the PCR mixture and a 532 nm continuous wave laser was used for heat generation,^[117] with

30 PCR cycles completed in 10 min at a rapid rate of heating and cooling.

Figure 12 shows ultrafast photonic PCR via plasmonic photothermal heating using low-cost LEDs under 450 nm illumination on gold films (120 nm thick).^[62] The system can complete 30 PCR cycles within 5 min in a 10 μL reaction volume due to the significant enhancement of the heating and cooling rates, up to 12.8 and 6.6 °C s^{-1} respectively. The blue LEDs with a peak emission wavelength of 450 nm exhibit highly efficient photothermal conversion. Furthermore, the use of an optical cavity created by two thin gold films for PCR can significantly improve the light absorption and the uniformity of the temperature distribution, compared with bottom-only heating.^[6] In addition, it has been reported that when suspended gold bipyramid nanoparticles are adopted in ultrafast real-time DNA amplification, their plasmon-resonant wavelength falls in the infrared (846 nm) region, which is far from the excitation and emission wavelengths of routine real-time PCR fluorescence, thus allowing more rapid and uniform heating without interfering with optical detection of the real-time PCR process.^[123]

Recently, the fastest ever PCR was achieved based on plasmonic heating, completing 30 PCR cycles in 54 s using dual-functional gold nanorods (Au-NRs) as both the heating source and the refractive index sensor.^[60] Alternative to gold for photonic PCR, other nanoparticles, such as Fe_3O_4 nanoclusters, can also be adopted. A system based on these achieved 30 PCR cycles in 7 min using an 808 nm, 460 mW NIR-CW laser diode, and the system can be coupled to a smartphone as a mobile-based photonic PCR device.^[61] The advances presented here will have an immediate impact on the development of

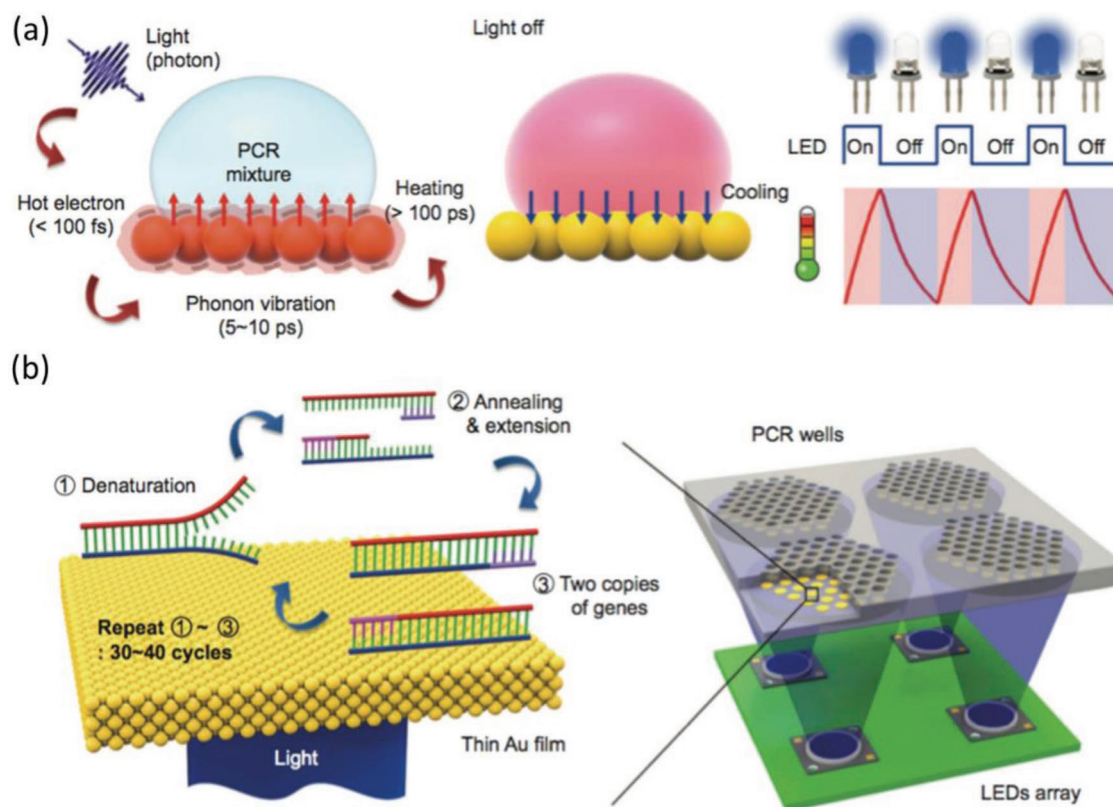


Figure 12. a) Schematic of the plasmonic photothermal heating of a PCR mixture through ultrafast photon–electron–phonon couplings. When the light is turned off, fast cooling of the heated solution is achieved by heat dissipation through the thin gold film. b) Schematics of the ultrafast photonic PCR thermocycler under excitation light from an LED array at two or three discrete temperatures. Each LED is modulated individually at different PCR annealing temperatures in multiple PCR reactions. Reproduced under the terms of Creative Commons Attribution 4.0 Unported License.^[62] Copyright 2015, Springer Nature.

plasmonic heating-assisted PCR, which will play a critical role in ultrafast point-of-care testing and diagnostics.

3.3.2. Manipulation of Biomaterials and Bioactivity

Compared with the manipulation of small objects, such as PS particles, through optothermal effects, the manipulation of living cells and other biomaterials is more important in medical science research, such as disease diagnosis, nanomedicine, and tissue engineering. Various living cells have been manipulated to different extents, including cellular movement and membrane activity. Recently, as shown in **Figure 13ab**, the development of optical thermophoresis and convection-assisted trapping schemes has enabled the long-range manipulation of various living organisms, such as bacteria and yeast cells, with an optical power 1000 times lower than that of optical tweezers.^[41,44]

In addition to living cell manipulation, the optothermal effect can also be applied in gene delivery and remote optical control of gene circuits. Because nucleic acid conjugation is weakened upon increasing local temperature, high spatiotemporal control of plasmonic structures allows localized gene release in the target intracellular environment.^[63] Photothermal heating can be used to change the localized permeability and the local membrane potential for gene entry into the cell, which

could potentially be applied in gene therapy.^[124,125] Although it is still unclear whether the gene carrier molecules or the flow of nucleic acids is guided into the cells by optothermal force, the combination of controlled membrane permeability and gene delivery has a high theragnostic potential.

Recently, the manipulation of cellular activity, such as light-mediated neuromodulation techniques, has become more popular in physiological and clinical applications, because its high spatial and temporal resolution deliver real benefits to neuroscience research.^[64–68] For example, as shown in **Figure 13c**, the reversible inhibition of neural spiking activity in a localized area was achieved via plasmonic gold nanorod-mediated photothermal stimulation under NIR illumination.^[68] Such optothermal assisted optofluidic systems provide a powerful neuromodulation tool to facilitate neuroscience research, including the investigation of complex neural networks with brain-like functions and development of treatments for neurological disorders.

4. Summary and Outlook

Thermal optofluidics has taken off as a burgeoning subfield of optofluidics. Plasmonic thermal effects offer tremendous possibilities in biomedical and clinical applications, enabling the

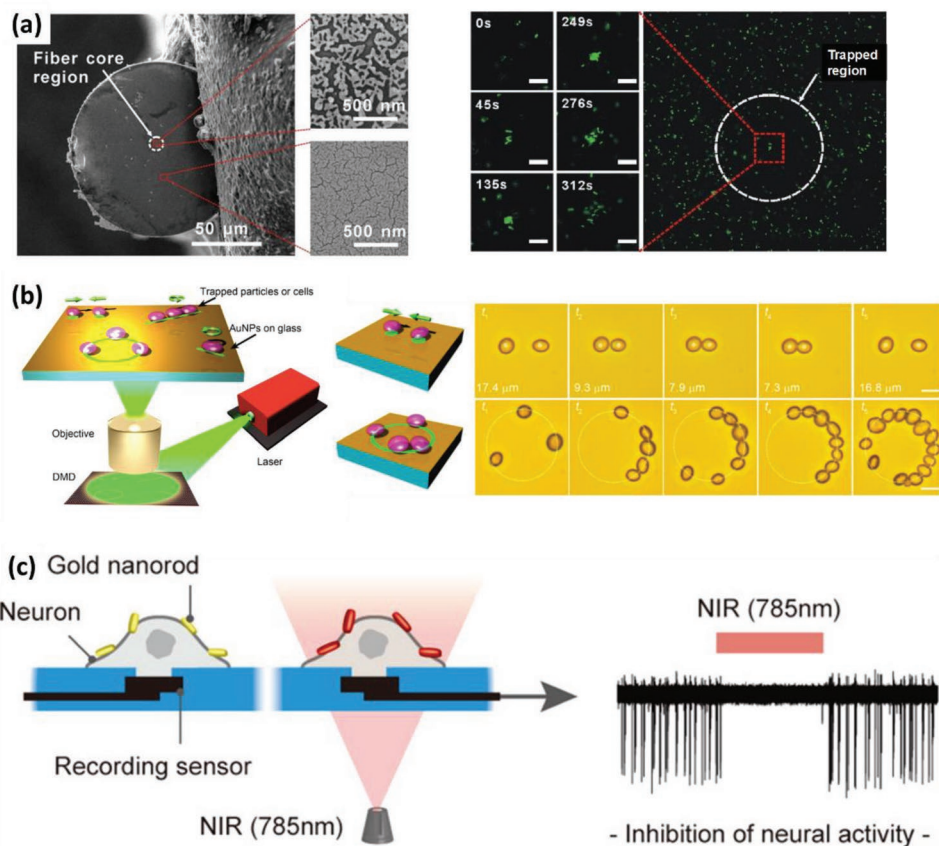


Figure 13. a) SEM image of a gold-coated fiber tip and time-lapse images of living *E. coli* cells with green fluorescence trapped in the fiber core region. b) Schematics of the optical setup and time-lapse images of digital micromirror-assisted thermophoretic tweezers for manipulating yeast cells. The tweezers are capable of the arbitrary spatial arrangement of multiple cells at a resolution of 100 nm. c) Schematics of the manipulation of neural activity with gold nanorod-mediated photothermal heating to inhibit the electrical activity of a neuron. a) Reproduced with permission.^[41] Copyright 2015, The Optical Society. b) Reproduced with permission.^[44] Copyright 2017, American Chemical Society. c) Reproduced with permission.^[68] Copyright 2014, American Chemical Society.

ultrafast remote control of nanoscale thermal distributions and dissipations. This review summarizes the physical principles behind thermal optofluidic applications, the mechanistic origin of heat by the plasmonic thermal effect, followed by the photothermal, thermodynamic, and hydrodynamic motions and forces induced by the heat source, i.e., natural convection, Marangoni convection, thermophoresis, the electrolyte Seebeck effect, depletion forces, interfacial effects in colloidal particles, and other interactions. The plasmonic thermal effect offers a significant tool to tailor the microscale or nanoscale temperature gradient together with the optical gradient in optofluidic systems. By designing on-demand plasmonic nanostructures, it is possible to create highly efficient and ultrafast (nano- to microseconds) thermodynamic motions on the nanoscale. In addition, the development of thermal optofluidics has effectively promoted low-power optofluidic applications in colloidal particle manipulation, optofluidic actuation techniques, and lab-on-a-chip bio-analysis applications. This review includes examples of applications in these three areas, which have in turn promoted the development and theoretical description of new physical phenomena. For example, although the research on the underlying physics of thermophoretic effects is still at an early stage, the experimental testing of various types of

colloidal systems with different kinds of chemical bonding and ionic species has gradually revealed the important role of the liquid–solid interfacial effects of colloidal particles.

For the future challenges and improvement of thermal optofluidic applications, with regard to colloidal particle manipulation, the nanoscale temperature gradient and optical gradient will both have an impact on the interfacial double layer of the colloidal particles. Therefore, on the one hand, one can advantageously tailor the temperature gradient field by using different optical modulation method. On the other hand, the key to realizing an on-demand particle manipulation scheme will rely on the ability of tailoring the interfacial layer between the particle and the liquid, such as designing different forms of interfacial chemical bonding, using partially metal-coated particles, varying the ion types in the solution, or applying different kinds of polymer solvent. These methods promise to realize the manipulation of different types of colloidal particles, including metallic nanoparticles, quantum dots, or particles of semiconductor materials. In addition, the scope of particle manipulation can be extended via waveguides, multiple-light-source manipulation, or other lab-on-a-chip devices to realize versatile strategies for particle trapping and assembling. With respect to optofluidic actuation techniques,

optothermal induced microbubbles are an emerging tool, thanks to their abilities to generate strong microscale Marangoni convection and optically controlled rapid gas expansion. The convective flow around the bubbles is influenced by the surrounding liquid and gas components. Further study of this convective flow will permit powerful actuation schemes to perform microscale optofluidic control. Regarding thermal optofluidics in biological applications, plasmonic substrates have shown unique advantages in areas of molecular diagnosis such as ultrafast PCR. Among the most promising directions for biological applications are optothermal assisted gene delivery and the treatment of neurological disorders. Since metallic nanoparticles are good biocompatible materials, thorough studies of their nanoscale thermodynamic interactions, behaviors under ultrafast optics, and interplays with biosamples in extremely small spatiotemporal dimensions, will advance the development of the technique for biochemical research and clinical applications.

In this review of optothermal manipulations and applications in optofluidic microsystems, we provide readers with an overview of the key features of this field. Looking forward, there is still considerable space for exploration to achieve the aforementioned potential of thermal optofluidic applications. Although most studies and applications are presently still within the scope of fundamental and academic fields, we believe that the study of thermal optofluidics will lead to the development of smart functional nanomaterials and point-of-care diagnostic devices or biosensors, which will benefit both materials science and healthcare.

Acknowledgements

The authors acknowledge funding support from the Research Grants Council, University Grants Committee HKSAR, through projects under General Research Fund (14210517) and Area of Excellence (AoE/P-02/12). The authors also gratefully acknowledge Professor Yu-Hwa Lo from Department of Electrical and Computer Engineering in University of California, San Diego for the advice of this paper.

Conflict of Interest

The authors declare no conflict of interest.

Keywords

biological manipulation, lab-on-a-chip devices, microfluidics, optofluidics, optothermal effect

Received: May 16, 2019

Revised: August 4, 2019

Published online: September 5, 2019

[1] V. R. Horowitz, D. D. Awschalom, S. Pennathur, *Lab Chip* **2008**, *8*, 1856.

[2] D. Erickson, C. Yang, D. Psaltis, *Photonics Spectra* **2008**, *42*, 74.

- [3] D. Psaltis, S. R. Quake, C. Yang, *Nature* **2006**, *442*, 381.
- [4] X. Fan, I. M. White, *Nat. Photonics* **2011**, *5*, 591.
- [5] M. D. Sonntag, J. M. Klingsporn, A. B. Zrimsek, B. Sharma, L. K. Ruvuna, R. P. Van Duyne, *Chem. Soc. Rev.* **2014**, *43*, 1230.
- [6] M. L. Brongersma, P. G. Kik, *Surface Plasmon Nanophotonics*, Vol. 131, Springer, Berlin **2007**.
- [7] K. Whang, J.-H. Lee, Y. Shin, W. Lee, Y. W. Kim, D. Kim, L. P. Lee, T. Kang, *Light: Sci. Appl.* **2018**, *7*, 68.
- [8] C. Escobedo, A. G. Brolo, R. Gordon, D. Sinton, *Nano Lett.* **2012**, *12*, 1592.
- [9] A. A. Yanik, M. Huang, O. Kamohara, A. Artar, T. W. Geisbert, J. H. Connor, H. Altug, *Nano Lett.* **2010**, *10*, 4962.
- [10] A. O. Govorov, W. Zhang, T. Skeini, H. Richardson, J. Lee, N. A. Kotov, *Nanoscale Res. Lett.* **2006**, *1*, 84.
- [11] C.-H. Chou, C.-D. Chen, C. C. Wang, *J. Phys. Chem. B* **2005**, *109*, 11135.
- [12] E. Hutter, J. H. Fendler, *Adv. Mater.* **2004**, *16*, 1685.
- [13] K. Jiang, D. A. Smith, A. Pinchuk, *J. Phys. Chem. C* **2013**, *117*, 27073.
- [14] G. Baffou, R. Quidant, F. J. García de Abajo, *ACS Nano* **2010**, *4*, 709.
- [15] H. H. Richardson, M. T. Carlson, P. J. Tandler, P. Hernandez, A. O. Govorov, *Nano Lett.* **2009**, *9*, 1139.
- [16] X. Chen, Y. Chen, M. Yan, M. Qiu, *ACS Nano* **2012**, *6*, 2550.
- [17] J. S. Donner, G. Baffou, D. McCloskey, R. Quidant, *ACS Nano* **2011**, *5*, 5457.
- [18] F. Winterer, C. M. Maier, C. Pernpeintner, T. Lohmüller, *Soft Matter* **2018**, *14*, 628.
- [19] A. S. Basu, Y. B. Gianchandani, *J. Micromech. Microeng.* **2008**, *18*, 115031.
- [20] K. Namura, K. Nakajima, M. Suzuki, *Nanotechnology* **2018**, *29*, 065201.
- [21] R. Piazza, A. Guarino, *Phys. Rev. Lett.* **2002**, *88*, 208302.
- [22] S. Iacopini, R. Piazza, *Europhys. Lett.* **2003**, *63*, 247.
- [23] A. Parola, R. Piazza, *Eur. Phys. J. E* **2004**, *15*, 255.
- [24] A. Ly, A. Majee, A. Würger, *New J. Phys.* **2018**, *20*, 025001.
- [25] K. Zhao, T. G. Mason, *Phys. Rev. Lett.* **2007**, *99*, 268301.
- [26] J. L. Anderson, D. C. Prieve, *Sep. Purif. Methods* **1984**, *13*, 67.
- [27] O. Stern, *Z. Elektrochem.* **1924**, *30*, 1014.
- [28] D. L. Chapman, *London Edinburgh Dublin Philos. Mag. J. Sci.* **1913**, *25*, 475.
- [29] H. V. Helmholtz, *Ann. Phys. Chem.* **1879**, *243*, 337.
- [30] M. Righini, A. S. Zelenina, C. Girard, R. Quidant, *Nat. Phys.* **2007**, *3*, 477.
- [31] M. L. Juan, M. Righini, R. Quidant, *Nat. Photonics* **2011**, *5*, 349.
- [32] B. J. Roxworthy, K. D. Ko, A. Kumar, K. H. Fung, E. K. Chow, G. L. Liu, N. X. Fang, K. C. Toussaint Jr., *Nano Lett.* **2012**, *12*, 796.
- [33] J. Berthelot, S. Aćimović, M. Juan, M. Kreuzer, J. Renger, R. Quidant, *Nat. Nanotechnol.* **2014**, *9*, 295.
- [34] M. L. Juan, R. Gordon, Y. Pang, F. Eftekhari, R. Quidant, *Nat. Phys.* **2009**, *5*, 915.
- [35] K. Wang, E. Schonbrun, P. Steinvurzel, K. B. Crozier, *Nat. Commun.* **2011**, *2*, 469.
- [36] M. Righini, P. Ghenuche, S. Cherukulappurath, V. Myroshnychenko, F. J. García de Abajo, R. Quidant, *Nano Lett.* **2009**, *9*, 3387.
- [37] J. C. Ndukaife, A. V. Kildishev, A. G. A. Nnanna, V. M. Shalae, S. T. Wereley, A. Boltasseva, *Nat. Nanotechnol.* **2016**, *11*, 53.
- [38] P. Kumari, J. Dharmadhikari, A. Dharmadhikari, H. Basu, S. Sharma, D. Mathur, *Opt. Express* **2012**, *20*, 4645.
- [39] Z. Kang, J. Chen, S.-Y. Wu, K. Chen, S.-K. Kong, K.-T. Yong, H.-P. Ho, *Sci. Rep.* **2015**, *5*, 9978.
- [40] Z. Kang, J. Chen, S.-Y. Wu, H.-P. Ho, *RSC Adv.* **2015**, *5*, 105409.
- [41] J. Chen, Z. Kang, S. K. Kong, H.-P. Ho, *Opt. Lett.* **2015**, *40*, 3926.

- [42] J. Chen, H. Cong, F.-C. Loo, Z. Kang, M. Tang, H. Zhang, S.-Y. Wu, S.-K. Kong, H.-P. Ho, *Sci. Rep.* **2016**, *6*, 35814.
- [43] H. Cong, J. Chen, H.-P. Ho, *Sens. Actuators, B* **2018**, *264*, 224.
- [44] L. Lin, X. Peng, X. Wei, Z. Mao, C. Xie, Y. Zheng, *ACS Nano* **2017**, *11*, 3147.
- [45] E. H. Hill, J. Li, L. Lin, Y. Liu, Y. Zheng, *Langmuir* **2018**, *34*, 13252.
- [46] L. Lin, X. Peng, M. Wang, L. Scarabelli, Z. Mao, L. M. Liz-Marzán, M. F. Becker, Y. Zheng, *ACS Nano* **2016**, *10*, 9659.
- [47] L. Lin, M. Wang, X. Peng, E. N. Lissek, Z. Mao, L. Scarabelli, E. Adkins, S. Coskun, H. E. Unalan, B. A. Korgel, *Nat. Photonics* **2018**, *12*, 195.
- [48] L. Lin, X. Peng, Z. Mao, X. Wei, C. Xie, Y. Zheng, *Lab Chip* **2017**, *17*, 3061.
- [49] A. Venancio-Marques, F. Barbaud, D. Baigl, *J. Am. Chem. Soc.* **2013**, *135*, 3218.
- [50] X. Miao, B. K. Wilson, L. Y. Lin, *Appl. Phys. Lett.* **2008**, *92*, 124108.
- [51] K. Abi-Samra, R. Hanson, M. Madou, R. A. GorkinIII, *Lab Chip* **2011**, *11*, 723.
- [52] J. L. Garcia-Cordero, D. Kurzbuch, F. Benito-Lopez, D. Diamond, L. P. Lee, A. J. Ricco, *Lab Chip* **2010**, *10*, 2680.
- [53] G. L. Liu, J. Kim, Y. Lu, L. P. Lee, *Nat. Mater.* **2006**, *5*, 27.
- [54] J. Chen, Z. Kang, G. Wang, J. F. C. Loo, S. K. Kong, H.-P. Ho, *Lab Chip* **2015**, *15*, 2504.
- [55] Z. Kang, J. Chen, H.-P. Ho, *Nanoscale* **2016**, *8*, 10266.
- [56] F. Tantussi, G. C. Messina, R. Capozza, M. Dipalo, L. Lovato, F. De Angelis, *ACS Nano* **2018**, *12*, 4116.
- [57] Y. Cheng, J. Yang, Z. Li, D. Zhu, X. Cai, X. Hu, W. Huang, X. Xing, *Appl. Phys. Lett.* **2017**, *111*, 151903.
- [58] C. Lv, S. N. Varanakkottu, T. Baier, S. Hardt, *Nano Lett.* **2018**, *18*, 6924.
- [59] H. Cong, F.-C. Loo, J. Chen, Y. Wang, S.-K. Kong, H.-P. Ho, *Biosens. Bioelectron.* **2019**, *133*, 236.
- [60] P. J. Roche, M. Najih, S. S. Lee, L. K. Beitel, M. L. Carnevale, M. Paliouras, A. G. Kirk, M. A. Trifiro, *Analyst* **2017**, *142*, 1746.
- [61] T.-J. Li, C.-M. Chang, P.-Y. Chang, Y.-C. Chuang, C.-C. Huang, W.-C. Su, D.-B. Shieh, *NPG Asia Mater.* **2016**, *8*, e277.
- [62] J. H. Son, B. Cho, S. Hong, S. H. Lee, O. Hoxha, A. J. Haack, L. P. Lee, *Light: Sci. Appl.* **2015**, *4*, e280.
- [63] H. Xin, B. Namgung, L. P. Lee, *Nat. Rev. Mater.* **2018**, *3*, 228.
- [64] K. Eom, C. Im, S. Hwang, S. Eom, T.-S. Kim, H. S. Jeong, K. H. Kim, K. M. Byun, S. B. Jun, S. J. Kim, *Biomed. Opt. Express* **2016**, *7*, 1614.
- [65] J. L. Carvalho-de-Souza, B. I. Pinto, D. R. Pepperberg, F. Bezanilla, *Biophys. J.* **2018**, *114*, 283.
- [66] J. L. Carvalho-de-Souza, J. S. Treger, B. Dang, S. B. Kent, D. R. Pepperberg, F. Bezanilla, *Neuron* **2015**, *86*, 207.
- [67] H. Nakatsuji, T. Numata, N. Morone, S. Kaneko, Y. Mori, H. Imahori, T. Murakami, *Angew. Chem.* **2015**, *127*, 11891.
- [68] S. Yoo, S. Hong, Y. Choi, J.-H. Park, Y. Nam, *ACS Nano* **2014**, *8*, 8040.
- [69] D. J. Griffiths, *Am. J. Phys.* **2005**, *73*, 574.
- [70] C. F. Bohren, D. R. Huffman, *Absorption and Scattering of Light by Small Particles*, John Wiley & Sons **2008**.
- [71] G. Chen, *J. Heat Transfer* **1996**, *118*, 539.
- [72] D. Ross, M. Gaitan, L. E. Locascio, *Anal. Chem.* **2001**, *73*, 4117.
- [73] R. Samy, T. Glawdel, C. L. Ren, *Anal. Chem.* **2008**, *80*, 369.
- [74] G. Yaralioglu, *Sens. Actuators, A* **2011**, *170*, 1.
- [75] V. Hohreiter, S. Wereley, M. Olsen, J. Chung, *Meas. Sci. Technol.* **2002**, *13*, 1072.
- [76] R. K. Benninger, Y. Koç, O. Hofmann, J. Requejo-Isidro, M. A. Neil, P. M. French, A. J. deMello, *Anal. Chem.* **2006**, *78*, 2272.
- [77] M. A. Bennet, P. R. Richardson, J. Arlt, A. McCarthy, G. S. Buller, A. C. Jones, *Lab Chip* **2011**, *11*, 3821.
- [78] G. Baffou, C. Girard, R. Quidant, *Phys. Rev. Lett.* **2010**, *104*, 136805.
- [79] G. Baffou, R. Quidant, C. Girard, *Appl. Phys. Lett.* **2009**, *94*, 153109.
- [80] E. Guyon, J.-P. Hulin, L. Petit, C. D. Matescu, *Physical Hydrodynamics*, Oxford University Press, Oxford **2001**.
- [81] M. Raffel, C. E. Willert, F. Scarano, C. J. Kähler, S. T. Wereley, J. Kompenhans, *Particle Image Velocimetry: A Practical Guide*, Springer, Berlin **2018**.
- [82] E. L. Koschmieder, *Bénard Cells and Taylor Vortices*, Cambridge University Press, Cambridge **1993**.
- [83] S. R. Palit, *Nature* **1956**, *177*, 1180.
- [84] R. Piazza, A. Parola, *J. Phys.: Condens. Matter* **2008**, *20*, 153102.
- [85] S. Dühr, D. Braun, *Appl. Phys. Lett.* **2005**, *86*, 131921.
- [86] S. Dühr, D. Braun, *Phys. Rev. Lett.* **2006**, *97*, 038103.
- [87] S. Dühr, D. Braun, *Proc. Natl. Acad. Sci. USA* **2006**, *103*, 19678.
- [88] M. Braibanti, D. Vigolo, R. Piazza, *Phys. Rev. Lett.* **2008**, *100*, 108303.
- [89] S. A. Putnam, D. G. Cahill, *Langmuir* **2005**, *21*, 5317.
- [90] K. A. Esfahian, A. Majee, M. Maskos, A. Würger, *Soft Matter* **2014**, *10*, 1931.
- [91] D. Vigolo, S. Buzzaccaro, R. Piazza, *Langmuir* **2010**, *26*, 7792.
- [92] E. Ruckenstein, *J. Colloid Interface Sci.* **1981**, *83*, 77.
- [93] M. Han, *J. Colloid Interface Sci.* **2005**, *284*, 339.
- [94] A. Würger, *Phys. Rev. Lett.* **2008**, *101*, 108302.
- [95] M. Reichl, M. Herzog, A. Götz, D. Braun, *Phys. Rev. Lett.* **2014**, *112*, 198101.
- [96] A. Majee, A. Würger, *Phys. Rev. Lett.* **2012**, *108*, 118301.
- [97] J. Agar, C. Mou, J. L. Lin, *J. Phys. Chem.* **1989**, *93*, 2079.
- [98] H. J. V. Tyrrell, *Diffusion and Heat Flow in Liquids*, Butterworth, London **1961**.
- [99] T. D. Edwards, M. A. Bevan, *Langmuir* **2012**, *28*, 13816.
- [100] D. Baranov, A. Fiore, M. van Huis, C. Giannini, A. Falqui, U. Lafont, H. Zandbergen, M. Zanella, R. Cingolani, L. Manna, *Nano Lett.* **2010**, *10*, 743.
- [101] M. Gouy, *J. Phys. Theor. Appl.* **1910**, *9*, 457.
- [102] R. J. Hunter, *Zeta Potential in Colloid Science: Principles and Applications*, Vol. 2, Academic Press, San Diego, CA **2013**.
- [103] P. Rodríguez-Sevilla, K. Prorok, A. Bednarkiewicz, M. I. Marqués, A. García-Martín, J. García Solé, P. Haro-González, D. Jaque, *Nano Lett.* **2018**, *18*, 602.
- [104] A. Ashkin, J. M. Dziedzic, T. Yamane, *Nature* **1987**, *330*, 769.
- [105] A. Ashkin, J. M. Dziedzic, J. Bjorkholm, S. Chu, *Opt. Lett.* **1986**, *11*, 288.
- [106] S. Kedenburg, M. Vieweg, T. Gissibl, H. Giessen, *Opt. Mater. Express* **2012**, *2*, 1588.
- [107] A. E. Larsen, D. G. Grier, *Nature* **1997**, *385*, 230.
- [108] T. M. Squires, M. P. Brenner, *Phys. Rev. Lett.* **2000**, *85*, 4976.
- [109] K. Svoboda, S. M. Block, *Annu. Rev. Biophys. Biomol. Struct.* **1994**, *23*, 247.
- [110] B. J. Roxworthy, K. C. Toussaint, *Opt. Express* **2012**, *20*, 9591.
- [111] K. C. Neuman, S. M. Block, *Rev. Sci. Instrum.* **2004**, *75*, 2787.
- [112] J. L. Anderson, *Annu. Rev. Fluid Mech.* **1989**, *21*, 61.
- [113] N. V. Churaev, B. V. Derjaguin, V. M. Muller, *Surface Forces*, Springer Science & Business Media, Berlin **2013**.
- [114] J. Chen, H. Cong, F.-C. Loo, Z. Kang, M. Tang, H. Zhang, S.-Y. Wu, S.-K. Kong, H.-P. Ho, *Sci. Rep.* **2016**, *6*, 35814.
- [115] C. M. Jin, W. Lee, D. Kim, T. Kang, I. Choi, *Small* **2018**, *14*, 1803055.
- [116] K. Zhang, A. Jian, X. Zhang, Y. Wang, Z. Li, H.-Y. Tam, *Lab Chip* **2011**, *11*, 1389.
- [117] K. Cao, Y. Liu, S. Qu, *Opt. Express* **2017**, *25*, 23690.
- [118] T.-H. Wu, L. Gao, Y. Chen, K. Wei, P.-Y. Chiou, *Appl. Phys. Lett.* **2008**, *93*, 144102.
- [119] J. Li, F. Zhao, Y. Deng, D. Liu, C.-H. Chen, W.-C. Shih, *Opt. Express* **2018**, *26*, 16893.

- [120] L. Lin, X. Peng, Z. Mao, W. Li, M. N. Yogeesh, B. B. Rajeeva, E. P. Perillo, A. K. Dunn, D. Akinwande, Y. Zheng, *Nano Lett.* **2016**, *16*, 701.
- [121] K. Namura, K. Nakajima, M. Suzuki, *Sci. Rep.* **2017**, *7*, 45776.
- [122] J. Zheng, X. Xing, J. Yang, K. Shi, S. He, *NPG Asia Mater.* **2018**, *10*, 340.
- [123] J.-H. Lee, Z. Cheglakov, J. Yi, T. M. Cronin, K. J. Gibson, B. Tian, Y. Weizmann, *J. Am. Chem. Soc.* **2017**, *139*, 8054.
- [124] P. Urban, S. R. Kirchner, C. Mühlbauer, T. Lohmüller, J. Feldmann, *Sci. Rep.* **2016**, *6*, 22686.
- [125] H. Jung, H. Kang, Y. Nam, *Biomed. Opt. Express* **2017**, *8*, 2866.